

Landing of a Quadrotor on a Moving Target Using Dynamic Image-Based Visual Servo Control

Pedro Serra, Rita Cunha, Tarek Hamel, David Cabecinhas, and Carlos Silvestre

Abstract—This paper addresses the landing problem of a vertical take-off and landing vehicle, exemplified by a quadrotor, on a moving platform using image-based visual servo control. Observable features on a flat and textured target plane are exploited to derive a suitable control law. The target plane may be moving with bounded linear acceleration in any direction. For control purposes, the image of the centroid for a collection of landmarks is used as position measurement, whereas the translational optical flow is used as velocity measurement. The proposed control law guarantees convergence to the desired landing spot on the target plane, without estimating any parameter related to the unknown height, which is also guaranteed to remain strictly positive. Moreover, convergence is guaranteed even in the presence of bounded and possibly time-varying disturbances, resulting, for example, from the motion of the target plane, measurement errors, or wind-induced force disturbances. To improve performance, an estimator for unknown constant force disturbances is also included in the control law. Simulation and experimental results are provided to illustrate and assess the performance of the proposed controller.

Index Terms—Automatic landing, dynamic image-based visual servo (IBVS) control, optical flow, unmanned aerial vehicle (UAV).

I. INTRODUCTION

THE automation of aerial vehicles is an important field of research, which has been growing in interest within the research community. While unmanned aerial vehicles (UAVs) have been used for decades, they are increasing in number and effectiveness, offering a wide range of applications intended to extend well beyond military use [1]. Noteworthy application examples include serving as platforms for antennas to provide connectivity access in remote places [2], inspection of infrastructures, road traffic supervision, victim localization, or movie shooting, to name a few of the possibilities. Catalyzing this trend is increasingly accurate and reliable technology in sensing, computational systems, and communication systems.

Accurately measuring the vehicle's position with respect to the local environment constitutes one of the major problems when designing motion control systems. A typical outdoor UAV sensor suite often includes a global positioning system, but it has some drawbacks as it does not work effectively indoors nor in urban canyon environments and provides positioning information in the Earth-centered, Earth-fixed frame without considering local topography.

Also included in the most common UAV's sensor suite is a lightweight and low-cost inertial measurement unit (IMU) system that can provide an effective estimation of attitude and angular velocity [3], [4]. However, for position and translational velocity, these systems are only capable of producing useful results for a few seconds due to the unbounded growth of the open-loop integration errors. One possibility to bound the error growth and render a full state estimation is to use an integrated vision system along with the IMU sensor [5], [6].

The integration of a vision system directly in the formulation of the control laws without attempting to estimate the position and velocity is denominated image-based visual servo (IBVS) control [7], [8]. The IBVS alternative approach is making headway within the research community. In contrast with traditional approaches that rely on reconstructing the state from the image sensor measurements, IBVS control methods make use of these measurements directly, which not only reduces computational complexity but also prevents adverse scaling effects that may result from computing the state using noisy measurements. Classical IBVS control algorithms were developed for robotic manipulators [9], [10], and due to their robustness with respect to errors in target geometry [11], several algorithms have been recently developed with application to aerial vehicles (see, for example, [12] and [13]), although the majority of those existing algorithms require the direct measurement of the translational velocity calling for an extra sensor. In [14], the authors write the dynamical model of a vertical take-off and landing (VTOL)

Manuscript received May 9, 2016; accepted July 27, 2016. Date of publication September 30, 2016; date of current version December 2, 2016. This paper was recommended for publication by Associate Editor D. Scaramuzza and Editor T. Murphey upon evaluation of the reviewers' comments. This work was partially supported by the Macao Science and Technology Development Fund (FDCT) under Grant FDCT/048/2014/A1; by Project MYRG2015-00126-FST from University of Macau; by Fundação para a Ciência e a Tecnologia (FCT) through Project UID/EEA/50009/2013 and Project PTDC/EEI-AUT/5048/2014; by the French Agence Nationale de la Recherche through Project ANR ASTRID SCAR under Grant ANR-12-ASTR-0033; and by the EQUIPEX project Robotex. The work of P. Serra and R. Cunha was supported by FCT through the Ph.D. Student Grant SFRH/BD/36696/2007 and the FCT Investigator Program under Contract IF/00921/2013, respectively.

P. Serra was with the Department of Electrical and Computer Engineering, Faculty of Science and Technology, University of Macau, Taipa, Macau. He is now with the Space Systems Business Unit, GMV Aerospace and Defense, 28760 Madrid, Spain (e-mail: pserra@isr.tecnico.ulisboa.pt).

R. Cunha is with the Institute for Systems and Robotics, Instituto Superior Técnico, Universidade de Lisboa, 1049-001 Lisbon, Portugal (e-mail: rita@isr.tecnico.ulisboa.pt).

T. Hamel is with I3S UNSA-CNRS, University of Nice Sophia Antipolis, 06103 Nice, France (e-mail: thamel@i3s.unice.fr).

D. Cabecinhas is with the Department of Electrical and Computer Engineering, Faculty of Science and Technology, University of Macau, Taipa, Macau, and also with the Institute for Systems and Robotics, Instituto Superior Técnico, Universidade de Lisboa, 1049-001 Lisbon, Portugal (e-mail: dcabecinhas@umac.mo).

C. Silvestre is with the Department of Electrical and Computer Engineering, Faculty of Science and Technology, University of Macau, Taipa, Macau, on leave from Instituto Superior Técnico, Universidade de Lisboa, 1049-001 Lisbon, Portugal (e-mail: csilvestre@umac.mo).

This paper has supplementary downloadable material available at <http://ieeexplore.ieee.org>, provided by the author. The material consists of a video, containing some of the tests that were performed within this work. Contact pserra@isr.ist.utl.pt for further information.

Digital Object Identifier 10.1109/TRO.2016.2604495

vehicle directly in the image space and develop a geometric visual controller that considers the second-order dynamics (in contrast with most visual servoing controllers that assume first-order dynamics).

There is a vast literature on the use of optical flow as a velocity measure for control purposes [15]. In [16], the authors propose an optical flow-based controller for automatic landing of a miniature aerial vehicle. An approach for wall collision avoidance using a depth map based on optical flow applied to small-scale helicopters is proposed in [17]. Optical flow-based control for landing a VTOL vehicle is proposed in [18], and for a fixed-wing vehicle in [19]. In [12], the authors use landmarks and optical flow to develop an adaptive control scheme for a flying vehicle.

In [20], the authors present an integrated control demonstration, in which a rotary wing UAV lands on a moving platform using vision-based localization of the target. The proposed controller uses the distance between the camera and the target, calculated using the size of the target in the image frame. Experimental results are presented with landings carried out onto stationary and moving targets in the field, under real conditions including the presence of wind and different, possibly adverse, lighting conditions.

This paper proposes a novel solution for the landing maneuver of a VTOL vehicle using IBVS control. The proposed controller uses a new centroid, inspired from [12] and [21], for position-like feedback and the translational optical flow, computed from the camera images, for velocity-like feedback. The kinematics of the system are represented in terms of the centroid vector and the translational optical flow, and as a consequence, input actuation is dependent on an unmeasured height that varies dynamically with the vehicle's and target's motion. In [12], this problem is overcome by introducing a virtual height dynamics along with adaptive estimation of the initial conditions. In this paper, the centroid vector is defined and used in a novel way to allow for the stabilization without the need to estimate parameters related to the unknown height. In [22], the authors propose a controller for landing on a moving target using the translational optical flow but without position feedback. Consequently, the vehicle lands anywhere, and the translational movement of the target plane is not considered. This paper goes a step further with the choice of the new centroid, defined in such way that enables the definition of a control law that guarantees convergence of the errors to zero, allowing the vehicle to land on a specific point on the moving target. The planar motion of the target is considered in this work, allowing for bounded linear accelerations, which widens the range of applicability of the proposed algorithm.

Following on previous work [23], which presents preliminary results using measurements from a VICON system [24], this paper improves the previous results by adding image processing to extract the translational optical flow from the image feed and providing an IBVS-IMU-aided control solution implemented fully onboard. Furthermore, in this paper, we show that the proposed control law exhibits the important property of completely rejecting bounded and possibly time-varying disturbances. In contrast with conventional control solutions, for which bounded disturbances may, at best, result in bounded errors, the present

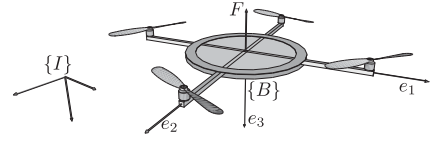


Fig. 1. Reference frames and force for schematic representation of a quadrotor.

solution guarantees convergence of the position errors (including the unknown height) and velocity errors in the presence of bounded disturbances. These gather several effects resulting, for example, from the motion of the target plane, measurement errors, and wind-induced forces. A relevant application scenario where we can take full advantage of this robustness property involves landing on a ship subject to effects of wind, waves, and sea currents.

The body of the paper consists of six sections followed by a conclusion. Section II presents the fundamental equations of motion of the dynamic model considered in this work. Section III describes the image features that are exploited and presents the image kinematics. Section IV introduces the proposed control strategy and the stability analysis. Section V describes simulations results, and, finally, Section VI shows some of the experimental results obtained. The paper concludes with some final comments in Section VII.

II. MODELING

Consider a quadrotor vehicle formed by a rigid cross-shaped frame equipped with four rotors, as shown in Fig. 1. The system can be modeled as a rigid body of mass m and tensor of inertia I , subject to external forces and moments [25]–[28].

To describe the motion of the quadrotor, two reference frames are introduced: the inertial reference frame $\{I\}$ fixed to the earth surface and associated with the vector basis $[e_1, e_2, e_3]$, and the body-fixed frame $\{B\}$ attached to the quadrotor's center of gravity and associated with the vector basis $[{}^B e_1, {}^B e_2, {}^B e_3]$. Let $(\xi, R) \in \mathbb{R}^3 \times SO(3)$ denote the configuration of $\{B\}$ with respect to $\{I\}$. Let V and Ω denote the translational and angular velocities, respectively, both expressed in $\{B\}$. Then, the kinematics and dynamics of a quadrotor vehicle can be written as

$$\dot{\xi} = RV \quad (1)$$

$$m\dot{V} = -m\Omega_{\times}V + F + R^T\mu_w \quad (2)$$

$$\dot{R} = R\Omega_{\times} \quad (3)$$

$$I\dot{\Omega} = -\Omega_{\times}I\Omega + \Gamma \quad (4)$$

where F and Γ , both expressed in $\{B\}$, are the force and torque applied to the vehicle, respectively. The matrix Ω_{\times} is a skew-symmetric matrix that satisfies $\Omega_{\times}b = \Omega \times b$, and the term μ_w , expressed in $\{I\}$, accounts for disturbances, for example due to wind, and unmodeled dynamics.

The force combines thrust and gravity components and can be described as

$$F = -T^B e_3 + mgR^T e_3 \quad (5)$$

where g is the gravitational acceleration, and T is the scalar thrust input, applied in the direction ${}^B e_3$, the third-axis unit vector $[0 \ 0 \ 1]^T$ of the body-fixed reference frame.

The simplest approach to overall vehicle control is to design a high-gain inner-loop controller for the system's attitude (3), (4). The inner-loop regulates the torque inputs to track a desired orientation $R_d(t)$. The desired orientation $R_d(t)$ is chosen to provide a thrust input with the adequate direction for the translational dynamics, which determines $r_{3d}(t) := R_d(t)e_3$, and a desired yaw angle for the remaining degree of freedom. More specifically, given a desired force F_d , (5) can be solved for T and $R = R_d$ up to a rotation around the z -axis. With a suitable high-gain inner-loop controller, the attitude dynamics is fast enough to assume that $R \approx R_d$ and, consequently, consider the translational dynamics described by (1) and (2), with control input directly given by $F = F_d$. The simplification is a common approach, used in practice and justified theoretically using small-gain arguments [29], [30]. Although it restricts the applicability of the results, in the context of the possible applications of this study, it is considered reasonable, since aggressive maneuvers are usually not desired during a normal landing operation.

III. IMAGE FEATURES

In this section, the image features used for control purposes are introduced and described in detail. Some assumptions regarding the environment and the setup are established.

Assumption 1: The camera is attached to the center of mass of the vehicle so that the camera reference frame coincides with the body-fixed reference frame.

The landing target lies on a textured plane called the target plane. Let ξ_T denote the position of a point on the target plane relative to the inertial frame $\{\mathcal{I}\}$, ${}^{\mathcal{I}}\eta$ the unit vector orthogonal to the plane, expressed in $\{\mathcal{I}\}$, and η the same unit vector expressed in $\{\mathcal{B}\}$, such that $\eta = R^T {}^{\mathcal{I}}\eta$. Notice that the pair $(\xi_T, {}^{\mathcal{I}}\eta)$ uniquely defines the target plane.

Assumption 2: The target plane can translate such that $v_T = \dot{\xi}_T \neq 0$, and its orientation is approximately constant such that ${}^{\mathcal{I}}\dot{\eta} = 0$. Moreover, it is assumed that the linear acceleration \dot{v}_T is bounded, and the target plane is horizontal, i.e., ${}^{\mathcal{I}}\eta = e_3$.

Under Assumption 2, the target plane is orthogonal to the gravitational acceleration vector. Since we are considering nonaggressive maneuvers, it is reasonable to assume that the IMU provides a good approximation for the gravitational acceleration expressed in $\{\mathcal{B}\}$ and, consequently, for $\eta = R^T e_3$.

Assumption 3: The features considered consist of a finite set of points lying on the target plane, which are called landmarks and are assumed to be visible at all times. Without loss of generality, it is also assumed that ξ_T gives the position of the centroid of the landmarks expressed in $\{\mathcal{I}\}$.

A. Spherical Projection

The image coordinates of the landmarks are provided by the vision system and passed to the control system. More specifically, a collection of 2-D pixel locations (X_i, Y_i) is provided and then transformed into spherical coordinates p_i called image points. These are 3-D points lying on a spherical image surface

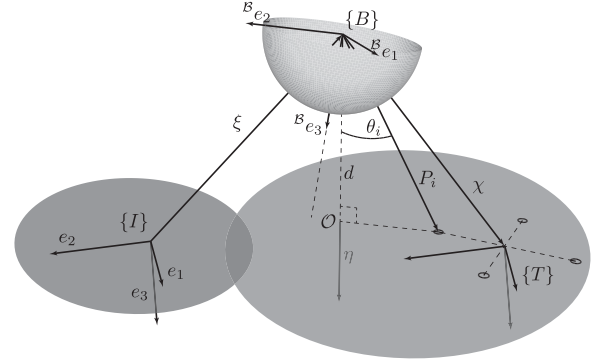


Fig. 2. Representation of the target plane and target constellations.

given by

$$p_i = \frac{P_i}{\|P_i\|} \in \mathbb{R}^3 \quad (6)$$

where P_i denote the position of the i th landmark relative to the body frame (see Fig. 2). Let s_i denote the position of the i th landmark relative to $\{\mathcal{I}\}$, which inherits the kinematics of the target plane, i.e., $\dot{s}_i = v_T$. Then, P_i can be described as

$$P_i = R^T (s_i - \xi). \quad (7)$$

B. Image Kinematics

An observed landmark inherits kinematics from the motion of both the vehicle and the target plane. From (1), (3), and (7), it is possible to write the kinematics of P_i as

$$\dot{P}_i = -\Omega_{\times} P_i - (V - V_T) \quad (8)$$

where $V_T = R^T v_T$ is the translational velocity of the target plane expressed in the body-fixed frame.

The kinematics of an image point, also called optical flow, can be derived from (6) using (8) and are described by [21], [31]

$$\dot{p}_i = -\Omega_{\times} p_i - \pi_{p_i} \frac{1}{\|P_i\|} (V - V_T) \quad (9)$$

where π_x denotes the projection operator defined for any $x \in \mathbb{S}^2 := \{x \in \mathbb{R}^3 : x^T x = 1\}$ as

$$\pi_x = I_3 - x x^T$$

such that for any $v \in \mathbb{R}^3$, $\pi_x v$ yields the projection of v onto the plane orthogonal to x . Let

$$d := \eta^T P_i \quad (10)$$

denote the height along the direction η between the vehicle and the target plane. Using the definition of the image point p_i , the height d can be rewritten as

$$d(t) = \eta^T p_i \|P_i\| = \cos \theta_i \|P_i\| \quad (11)$$

where θ_i is the angle between η and p_i (see Fig. 2).

C. Visual Position Measurement

The visual feature used for control purposes that encodes information about the position of the vehicle relative to the

target plane is the centroid vector given by

$$q := \frac{1}{n} \sum_{i=1}^n \frac{p_i}{\eta^T p_i} \in \mathbb{R}^3 \quad (12)$$

where $n \geq 1$ is the number of landmarks. Substituting (6) and (12) into (13) yields

$$q = \frac{\chi}{d}$$

where χ denotes the position of the landmarks' centroid relative to the body frame given by

$$\chi = \frac{1}{n} \sum_{i=1}^n P_i$$

(see Fig. 2). According to (7) and Assumption 2, χ can also be written as

$$\chi = R^T (\xi_T - \xi)$$

with time derivative given by

$$\dot{\chi} = -\Omega_{\times} \chi - (V - V_T). \quad (13)$$

Remark 1: For the particular case of a landing maneuver under consideration, the goal is to drive χ to zero, i.e., land on the centroid of the landmarks.

Remark 2: While q is measurable from the image, the 3-D position vector χ and also the height d remain unknown for the IBVS control system.

D. Visual Velocity Measurement—Translational Optical Flow

The visual velocity measurement that is used in the following is the translational optical flow given by

$$W(t) = \frac{V(t) - V_T(t)}{d(t)}.$$

When the observed world is a planar surface, translational optical flow has two components: the flow in the two coplanar directions, analogous to classical optical flow, and the flow in the normal direction to the plane, analogous to optical divergence [22].

Using (11) in (9), the optical flow of an image point p under spherical projection and expressed in $\{\mathcal{B}\}$ can be described by

$$\dot{p} = -\Omega_{\times} p - \cos \theta \pi_p W.$$

An effective measurement of W is obtained from the integral of the observed optical flow over the solid area \mathcal{W}^2 of the lower hemisphere of the sphere \mathcal{S}^2 corresponding to the visual image of a region of the target plane, with central point \mathcal{O} , the intersection of the normal line to the target plane that passes through the origin of $\{\mathcal{B}\}$ (see Fig. 3).

Consider the integral of \dot{p} over the solid area \mathcal{W}^2 defined by

$$\begin{aligned} \phi_w &= \int \int_{\mathcal{W}^2} \dot{p} \, dp \\ &= \int_0^{2\pi} \int_{\theta_0}^{\theta_1} (-\Omega_{\times} p - \cos \theta \pi_p W) \sin \theta \, d\theta \, d\alpha \end{aligned}$$

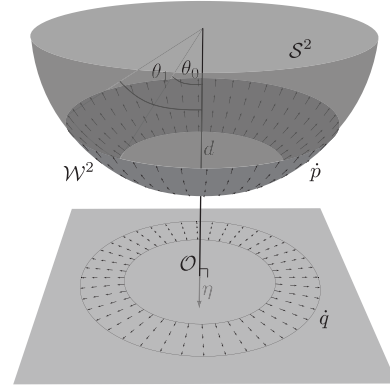


Fig. 3. Translational optical flow computation.

where the image point p is described in polar coordinates by

$$p = R^T \begin{bmatrix} \sin \theta \cos \alpha \\ \sin \theta \sin \alpha \\ \cos \theta \end{bmatrix}.$$

The angles θ_0 and θ_1 define the area of integration (see Fig. 3); hence, $0 \leq \theta_0 < \theta_1$ and $\theta_1 \leq \frac{\pi}{2}$. The choice of the values for θ_0 and θ_1 is a degree of freedom for optimizing the practical implementation of the algorithm. Increasing θ_0 results in ignoring the points close to \mathcal{O} which do not carry much information since their velocities projected onto the sphere are approximately 2-D vectors and will also reduce the computational cost of solving the integral. In addition, the value of θ_1 is related to the field of view of the camera and, in practice, cannot be very high (i.e., close to $\frac{\pi}{2}$). On the other hand, a larger integral area, in principle, reduces the effect of noise on the estimation.

Lengthy but straightforward computations show that

$$\phi_w = -\frac{\pi}{2} (\cos 2\theta_0 - \cos 2\theta_1) \Omega_{\times} \eta + R^T \Lambda R W \quad (14)$$

where

$$\Lambda =$$

$$\frac{\pi}{32} \text{diag} \left\{ \begin{bmatrix} 12 \cos 2\theta_0 - 12 \cos 2\theta_1 + \cos 4\theta_0 - \cos 4\theta_1 \\ 12 \cos 2\theta_0 - 12 \cos 2\theta_1 + \cos 4\theta_0 - \cos 4\theta_1 \\ 16 \sin^4 \theta_1 - 16 \sin^4 \theta_0 \end{bmatrix} \right\}.$$

Solving (14) to obtain W yields

$$W = -R^T \Lambda^{-1} R \left(\phi_w + \frac{\pi}{2} (\cos 2\theta_0 - \cos 2\theta_1) \Omega_{\times} \eta \right). \quad (15)$$

Measuring the optical flow constitutes a fundamental aspect for a practical implementation of the algorithm proposed in the following. Among others, the Lucas–Kanade algorithm [32] allows us to obtain the 2-D optical flow field of a specific set of feature points resulting in a set of velocities. Let $P = [X \ Y \ Z]^T$ denote the body coordinates of a landmark, where we omit the subscript i to lighten notation, and let $\bar{p} = [x \ y \ 1]^T$ denote the corresponding planar image point, defined such that $x = X/Z$ and $y = Y/Z$. Then, the spherical image point p can be obtained

by projecting \bar{p} into the unit sphere, i.e., $p = \frac{\bar{p}}{\|\bar{p}\|}$. Thus

$$\dot{p} = \frac{1}{\|\bar{p}\|} \pi_{\bar{p}} \dot{\bar{p}}$$

where $\dot{\bar{p}} = [\dot{x} \ \dot{y} \ 0]^T$ is the 2-D optical flow obtained from the image using extraction methods usually available within the most common image processing libraries such as OpenCV [33], or using dedicated optical flow sensors [16], [34], [35].

IV. VISION-BASED CONTROL

In this section, we consider the problem of defining an IBVS controller to perform the landing maneuver. Using the inner-loop control strategy described in Section II, the control objective for the outer-loop system consists in designing a feedback law for the force F , using measurements of the centroid q , the translational optical flow W , and the normal to the target η , such that χ converges to zero and V to V_T . Simultaneously, a strong physical constraint is imposed by the environment on the height d between the vehicle and the desired landing spot, for it has to be strictly positive at all times. To guarantee a smooth landing, the controller must ensure that $d = 0$ is asymptotically reached with zero velocity. This obvious constraint, together with the fact that d is unknown, adds complexity to the control problem and requires careful consideration in the stability analysis.

Defining the relative velocity

$$\tilde{V} := V - V_T$$

using (2) and (13), the error kinematics and dynamics can be described as

$$\begin{cases} \dot{\chi} = -\Omega_{\times} \chi - \tilde{V} \\ \dot{\tilde{V}} = -\Omega_{\times} \tilde{V} + \frac{1}{m} F + R^T (\mu_w - \mu_T) \end{cases} \quad (16)$$

where μ_T denotes the target plane linear acceleration, expressed in $\{\mathcal{I}\}$, i.e., $\mu_T = \dot{v}_T$.

Consider the control law

$$\frac{1}{m} F = -\pi_{\eta} k_1 (k_2 W - q) + k_3 \eta (w_d - \eta^T W) + \mu_m \quad (17)$$

where (k_1, k_2, k_3) are positive gains, $w_d > 0$, and μ_m accounts for measurement noise, which is assumed to be bounded and gathers errors related to measurement of the gravitational acceleration direction, target plane direction η , translational optical flow W , and landmark centroid vector q .

Theorem 1: Consider the system (16) in closed loop with the control law (17) and define the bounded disturbance vector μ as

$$\mu := \mu_m + R^T (\mu_w - \mu_T). \quad (18)$$

If $d_0 := d(0) > 0$ and the condition

$$k_3 w_d > \max\{|\eta^T \mu(t)|\} + \epsilon \quad (19)$$

holds for all $t \geq 0$ and $\epsilon > 0$ arbitrarily small, then for all $t \geq 0$, the solutions to the system exist and

- 1) the height $d(t)$ is positive and bounded and converges exponentially fast to zero;

- 2) the state $(\chi(t), \tilde{V}(t))$ is bounded and converges exponentially fast to zero.

Proof. Proof of item 1: From (10), the height d can also be described as $d = \eta^T \chi$. It follows that the first time derivative of d can be written as $\dot{d} = -\eta^T \tilde{V}$, and the dynamics of d is described by

$$\ddot{d} = -k_3 \left(\frac{\dot{d}}{d} + w_d \right) - \mu_{\eta}$$

where $\mu_{\eta} = \eta^T \mu$. The proof of convergence for this kind of system was presented in [22]; hence, this paper describes an alternative proof and the interested reader is referred to [22]. Consider the change of variables where the first state d remains unchanged and the second state is defined as

$$\lambda(t) = d(t) \exp \left\{ \frac{\dot{d}(t)}{k_3} \right\}. \quad (20)$$

The new system is described by

$$\dot{d}(t) = -k_3 (\log d(t) - \log \lambda(t)) \quad (21)$$

$$\dot{\lambda}(t) = -\frac{k_3 w_d + \mu_{\eta}(t)}{k_3} \lambda(t) \quad (22)$$

which is well defined if $d(t) > 0$ and $\lambda(t) > 0$. If (19) holds, it immediately follows from (22) that $\lambda(t)$ converges to zero with solution given by

$$\lambda(t) = \lambda_0 \exp \left\{ -\frac{1}{k_3} \int_0^t \mu_{\eta}(\tau) d\tau - w_d t \right\}, \quad \lambda_0 = \lambda(0)$$

and is upper and lower bounded by exponentials, i.e.,

$$\lambda_0 \exp\{-c_1 t\} \leq \lambda(t) \leq \lambda_0 \exp\{-c_2 t\} \quad (23)$$

where $c_1 = w_d + \frac{1}{k_3} \max\{|\mu_{\eta}(t)|\}$ and $c_2 = w_d - \frac{1}{k_3} \max\{|\mu_{\eta}(t)|\}$. Meaning that, if $\lambda_0 > 0$ or equivalently $d_0 > 0$, then $\lambda(t) > 0$ for all $t > 0$.

Analyzing (21), the following three scenarios may occur:

- a) $\dot{d}(t) > 0$, if $d(t) < \lambda(t)$
- b) $\dot{d}(t) < 0$, if $d(t) > \lambda(t)$
- c) $\dot{d}(t) = 0$, if $d(t) = \lambda(t)$

and also

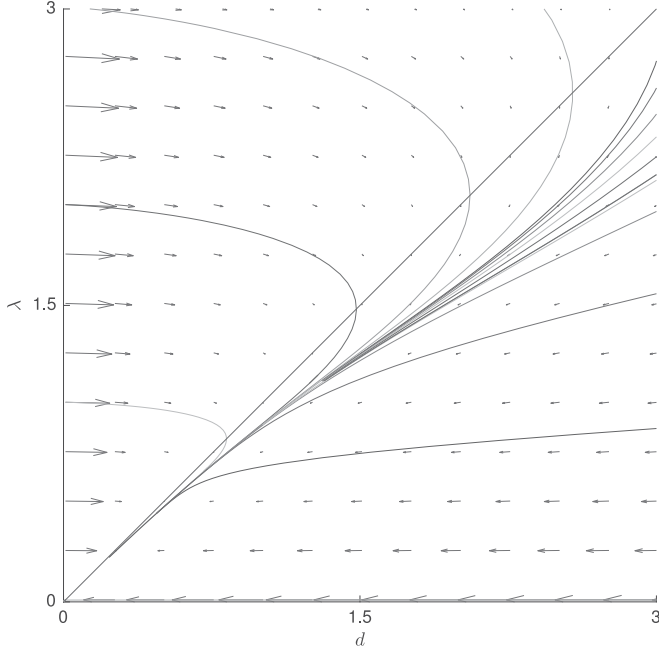
$$\lim_{\lambda \rightarrow 0, d \neq 0} \dot{d}(t) = -\infty$$

$$\lim_{d \rightarrow 0, \lambda \neq 0} \dot{d}(t) = +\infty.$$

If $d_0 < \lambda_0$, then $d(t)$ increases, while $\lambda(t)$ is decreasing to zero, meaning there exists a time $T_1 \geq 0$ such that $d(T_1) = \lambda(T_1)$ and $d(t)$ cannot grow unbounded. After crossing the line $d = \lambda$ at $t = T_1$, $d(t > T_1)$ starts decreasing together with $\lambda(t > T_1)$ and both converge monotonically to zero, without crossing either the line $d = \lambda$ or the line $d = 0$, as shown in Fig. 4.

To show that $\dot{d}(t)$ also converges to zero, consider the storage function

$$\mathcal{L}_1 = \frac{1}{2} d^2$$

Fig. 4. Phase portrait of the evolution of the state (d, λ) .

with time derivative given by

$$\dot{\mathcal{L}}_1 = -k_3 \dot{d} \left(\frac{\dot{d}}{d} + w_d + \frac{\mu_\eta}{k_3} \right). \quad (24)$$

Then, as long as

$$|\dot{d}| > \left(w_d + \frac{\mu_\eta}{k_3} \right) d$$

the function \mathcal{L}_1 is decreasing, meaning that $|\dot{d}|$ is bounded. Since $d(t)$ is converging to zero, one can also conclude from (24) that \dot{d} is converging to zero. Moreover, substituting (20) into (23) for $t \geq T_1$, $d(t)$ can also be bounded by exponentials

$$0 < \sigma_1 d_0 \exp\{-c_1 t\} \leq d(t) \leq \sigma_2 d_0 \exp\{-c_2 t\}$$

where

$$\sigma_1 = \exp \left\{ \frac{1}{k_3} (\dot{d}(0) - \max\{\dot{d}(t)\}) \right\}$$

$$\sigma_2 = \exp \left\{ \frac{1}{k_3} (\dot{d}(0) - \min\{\dot{d}(t)\}) \right\}$$

showing that, for $t > T_1$, $d(t)$ converges exponentially to zero and, given (24), so does $\dot{d}(t)$.

Proof of item 2: We have shown that $(d, \dot{d}) = (\eta^T \chi, -\eta^T \tilde{V})$ converges exponentially fast to zero. It remains to be proven that $(\pi_\eta \chi, \pi_\eta \tilde{V})$ also converges to zero. Let

$$\begin{bmatrix} \chi_1 & \tilde{V}_1 & \mu_1 \end{bmatrix} = \pi_\eta \begin{bmatrix} \chi & \tilde{V} & \mu \end{bmatrix}$$

and consider the closed-loop system

$$\begin{cases} \dot{\chi}_1 = -\Omega_\times \chi_1 - \tilde{V}_1 \\ \dot{\tilde{V}}_1 = -\Omega_\times \tilde{V}_1 - k_1 \frac{\delta}{d} + \mu_1 \end{cases}$$

where

$$\delta = k_2 \tilde{V}_1 - \chi_1.$$

Consider also the storage function

$$\mathcal{L}_2 = \frac{1}{2} \|\chi_1\|^2 + \frac{1}{2} \|\delta\|^2 + \frac{d}{k_1} \|\tilde{V}_1\|^2$$

with time derivative given by

$$\begin{aligned} \dot{\mathcal{L}}_2 = & -\frac{1}{k_1} (k_1 k_2 - \dot{d}) \|\tilde{V}_1\|^2 - \frac{k_1 k_2}{d} \|\delta\|^2 \\ & + k_2 \delta^T \mu_1 + 2 \frac{d}{k_1} \tilde{V}_1^T \mu_1. \end{aligned}$$

Since $\dot{d}(t)$ and $\mu_1(t)$ are bounded, it follows that the state (χ_1, \tilde{V}_1) , or equivalently (χ_1, δ) , cannot grow unbounded in finite time.

Consider now the storage function

$$\mathcal{L}_3 = \frac{k_2}{2} \frac{\delta^T \delta}{d^2}$$

with time derivative given by

$$\dot{\mathcal{L}}_3 = -\frac{\delta^T}{d^2} \left[(k_1 k_2^2 + k_2 \dot{d} - d) \frac{\delta}{d} - \chi_1 + \mu_1 \right].$$

From item 1, we can ensure that there exists a finite time T_1 , after which $k_1 k_2^2 + k_2 \dot{d}(t) - d(t) > \epsilon > 0$ so that $\dot{\mathcal{L}}_3 < 0$ as long as

$$\frac{\|\delta\|}{d} > \frac{1}{\epsilon} (\|\chi_1\| + \|\mu_1\|)$$

which, in turn, implies that $\frac{\delta}{d}$ is bounded. Using the fact that d is converging to zero exponentially, it follows that δ is also converging to zero exponentially. To show that χ_1 is also converging to zero, note that the system with state χ_1 can be rewritten as

$$\dot{\chi}_1 = -\Omega_\times \chi_1 - \frac{1}{k_2} \chi_1 - \frac{1}{k_2} \delta$$

which is input-to-state stable with a vanishing input given by δ . ■

Remark 3: Notice that the only condition imposed on the gains is given by (19), which involves k_3 and w_d . Thus, the disturbance term μ_1 , which is orthogonal to η , can be rejected irrespective of the choice of k_1 and k_2 . Given the definition of $\delta = k_2 \tilde{V}_1 - \chi_1$, the term $\frac{1}{k_2} \chi_1$ can be interpreted as the desired value for \tilde{V}_1 , indicating that for fast convergence, k_2 should be small. Notice also that the adjustable scalar $w_d > 0$ can be interpreted as the desired translational optical flow in the η -direction.

A. Adding an Estimator for an Unknown Constant Inertial Force

Consider now that the unknown target acceleration μ_T and the unknown force μ_w in (2), due to wind and/or unmodeled dynamics, can be decomposed into constant and time-varying

terms, and let

$$\mu_c := \pi_\eta R^T (\mu_{w_c} - \mu_{T_c})$$

$$\mu_v := \pi_\eta R^T (\mu_{w_v} - \mu_{T_v})$$

denote the body-fixed frame representations of these constant and time-varying components that are parallel to the target plane. Notice that according to this definition

$$\dot{\mu}_c = -\Omega_\times \mu_c.$$

Then, the error system (16) can be rewritten as

$$\begin{cases} \dot{\chi} = -\Omega_\times \chi - \tilde{V} \\ \dot{\tilde{V}} = -\Omega_\times \tilde{V} + \frac{1}{m} F + \mu_c + \mu_v + \eta \eta^T R^T (\mu_T + \mu_w). \end{cases} \quad (25)$$

In addition, let $\hat{\mu}_c$ be an estimate of μ_c and define the estimate error as

$$\tilde{\mu}_c := \mu_c - \hat{\mu}_c.$$

Proposition 1: Consider the system (25) in closed loop with the control law

$$\frac{1}{m} F = -\pi_\eta k_1 (k_2 W - q) + k_3 \eta (w_d - \eta^T W) - \hat{\mu}_c + \mu_m \quad (26)$$

and estimator dynamics

$$\dot{\hat{\mu}}_c = -\Omega_\times \hat{\mu}_c + \pi_\eta k_4 \left((k_2 W - q) - \frac{1}{k_1} \mu_m \right)$$

where (k_1, k_2, k_3, k_4) are positive gains, and w_d is the desired translational optical flow in the η -direction. If the initial condition is such that $d_0 := d(0) > 0$, the gain k_4 is such that

$$k_4 < \frac{k_1}{k_2} \quad (27)$$

and the condition

$$k_3 w_d > \max\{|\eta^T \mu(t)|\} + \epsilon$$

holds for all $t \geq 0$ and $\epsilon > 0$ arbitrarily small with $\mu(t)$ given by (18), then for all $t \geq 0$, the solutions to the system exist and

- 1) the height $d(t)$ is positive and bounded for all $t > 0$ and converges exponentially fast to zero;
- 2) the state $(\chi, \tilde{V}, \tilde{\mu}_c)$ is bounded for all $t > 0$ and converges exponentially fast to zero.

Proof. Proof of item 1: The proof is analogous to the proof of item 1 of Theorem 1.

Proof of item 2: Define the change of variables

$$\delta = k_2 \tilde{V}_1 - \chi_1$$

and consider the closed-loop system

$$\begin{cases} \dot{\chi}_1 = -\Omega_\times \chi_1 - \frac{1}{k_2} \delta - \frac{1}{k_2} \chi_1 \\ \dot{\delta} = -\Omega_\times \delta - k_2 \left(\frac{k_1}{d} \delta - \pi_\eta \mu_m \right) + \frac{1}{k_2} \delta + \frac{1}{k_2} \chi_1 \\ \quad + k_2 \tilde{\mu}_c + k_2 \mu_v. \\ \dot{\tilde{\mu}}_c = -\Omega_\times \tilde{\mu}_c - \frac{k_4}{k_1} \left(\frac{k_1}{d} \delta - \pi_\eta \mu_m \right). \end{cases}$$

Define the following Lyapunov function candidate

$$\mathcal{L}_4 = \frac{1}{2} \|\chi_1\|^2 + \frac{1}{2} \|\delta\|^2 + \frac{k_1 k_2}{2 k_4} \|k_2 \tilde{\mu}_c\|^2 - k_2^2 \tilde{\mu}_c^T \delta,$$

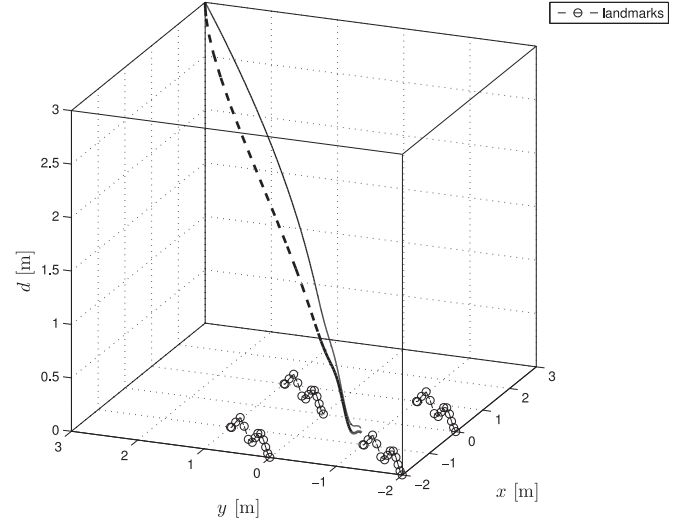


Fig. 5. Trajectories in 3-D space (x, y, d) . Solid lines correspond to initial velocity $V(0) = [0 \ 0 \ 0]^T \text{ ms}^{-1}$. Dashed lines correspond to initial velocity $V(0) = [0 \ 0 \ 1]^T \text{ ms}^{-1}$. The trajectories of the four landmarks are also plotted with circle markers.

which is positive definite provided that condition (27) is satisfied. The time derivative of \mathcal{L}_4 is given by

$$\begin{aligned} \dot{\mathcal{L}}_4 = & -\frac{1}{k_2} \|\chi_1\|^2 - k_2 \|k_2 \tilde{\mu}_c\|^2 - k_2 \tilde{\mu}_c^T \chi_1 \\ & - \frac{1}{k_2 d} (k_2^2 (k_1 - k_4 k_2) - d) \|\delta\|^2 \\ & + k_2 \left(1 - \frac{k_2 k_4}{k_1} \right) \delta^T \mu_m + k_2 \delta^T \mu_v. \end{aligned}$$

Since all the exogenous terms are bounded, we can conclude that $(\chi_1, \delta, \tilde{\mu}_c)$ cannot grow unbounded in finite time. Using arguments similar to those in the proof of Theorem 1, we can also show that $\frac{\delta}{d}$ is bounded, and consequently, δ and χ_1 are converging to zero exponentially fast. From the time derivative of \mathcal{L}_4 , it also follows that there exists a time $T > 0$, after which

$$d(t) < k_2^2 (k_1 - k_4 k_2)$$

and the term on $\frac{1}{d} \|\delta\|^2$ becomes negative. As $d(t)$ decreases, the cross terms due to the disturbances μ_m and μ_v are dominated by this negative term on $\frac{1}{d} \|\delta\|^2$, and we can conclude that the whole state, including $\tilde{\mu}_c$, is converging to zero. ■

Remark 4: Notice that imposing condition (27) on k_4 is not very restrictive, since this gain is being applied to the integral term and thus should be kept small. The boundedness of $\frac{\delta}{d}$ is also relevant to ensure that the integral state $\hat{\mu}_c$ does not grow very large.

V. SIMULATION RESULTS

In this section, simulation results are shown to illustrate the behavior of the closed-loop system using the landing controller (26) on top of a high-gain inner-loop attitude controller. In the conducted simulations, two initial velocities were considered $V(0) = [0 \ 0 \ 0]^T \text{ ms}^{-1}$ (represented by solid lines) and

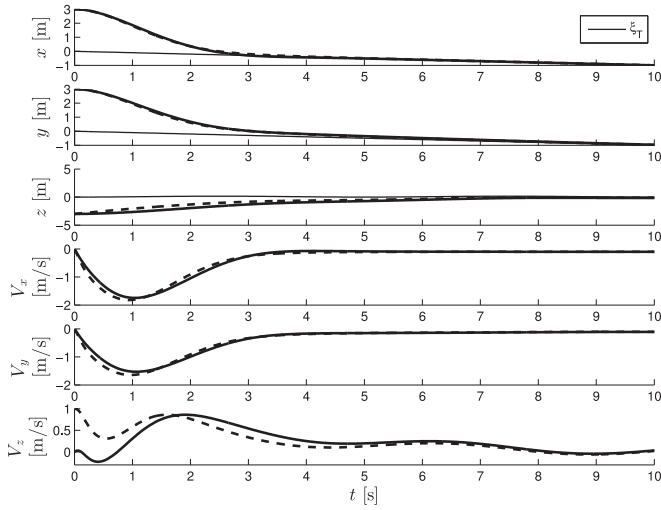


Fig. 6. Evolution of $\xi(t)$ and $V(t)$. Solid lines correspond to initial velocity $V(0) = [0 \ 0 \ 0]^T \text{ ms}^{-1}$. Dashed lines correspond to initial velocity $V(0) = [0 \ 0 \ 1]^T \text{ ms}^{-1}$.

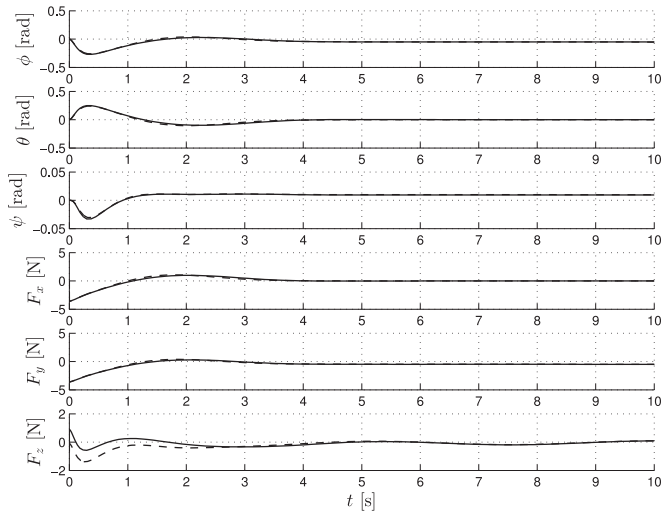


Fig. 7. Evolution of the Euler angles (φ, ϑ, ψ) and of the control actuation F , with time. Solid lines correspond to initial velocity $V(0) = [0 \ 0 \ 0]^T \text{ ms}^{-1}$. Dashed lines correspond to initial velocity $V(0) = [0 \ 0 \ 1]^T \text{ ms}^{-1}$.

$V(0) = [0 \ 0 \ 1]^T \text{ ms}^{-1}$ (represented by dashed lines). The initial position is $\xi(0) = [3 \ 3 \ -5]^T \text{ m}$, and the unknown constant force is $\mu_c = [0 \ 0.5 \ 0]^T \text{ N}$. Four landmarks were placed on initial positions $s_1 = [1 \ 1 \ 0]^T \text{ m}$, $s_2 = [1 \ -1 \ 0]^T \text{ m}$, $s_3 = [-1 \ 1 \ 0]^T \text{ m}$, and $s_4 = [-1 \ -1 \ 0]^T \text{ m}$ with respect to the inertial frame and with velocity $v_T = [-0.1 \ -0.1 \ 0.1 \sin(2\pi t/5)]^T \text{ ms}^{-1}$. The choice of gains was $k_1 = 3.5$, $k_2 = 4$, $k_3 = 3$, $k_4 = 0.5$, and $w_d = 0.3 \text{ s}^{-1}$.

Fig. 5 depicts the trajectory in 3-D space performed by the vehicle and Fig. 6 the position and velocity evolution with time. The chosen target velocity emulates the landing on a platform that is moving forward with a constant speed and up and down following a sinusoidal profile. One possible application that can roughly be described by this velocity profile is the landing on a

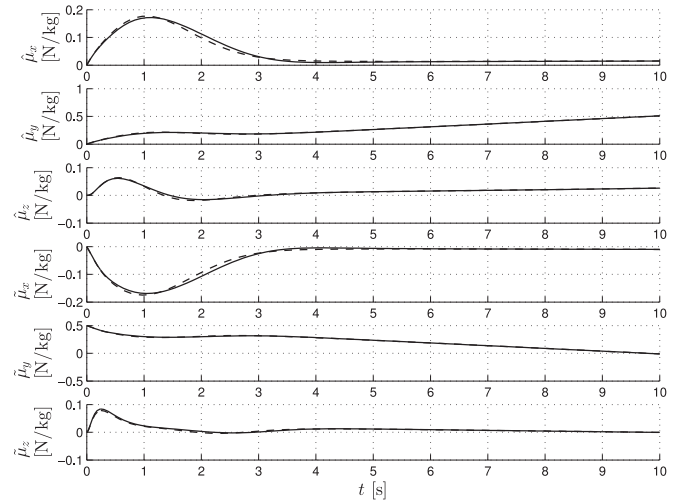


Fig. 8. Evolution of the estimator $\hat{\mu}_c(t)$ and of the estimation error $\tilde{\mu}_c(t)$ with time. Solid lines correspond to initial velocity $V(0) = [0 \ 0 \ 0]^T \text{ ms}^{-1}$. Dashed lines correspond to initial velocity $V(0) = [0 \ 0 \ 1]^T \text{ ms}^{-1}$.

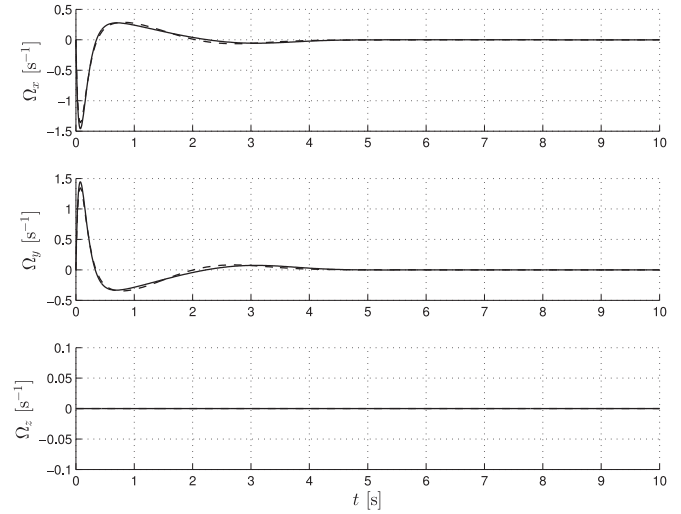


Fig. 9. Evolution of $\Omega(t)$ in time. Solid lines correspond to initial velocity $V(0) = [0 \ 0 \ 0]^T \text{ ms}^{-1}$. Dashed lines correspond to initial velocity $V(0) = [0 \ 0 \ 1]^T \text{ ms}^{-1}$.

floating vessel that is moving forward and suffering the influence of waves.

Fig. 7 illustrates the evolution of the Euler angles (φ, ϑ, ψ) computed from the rotation matrix R and of the control actuation F over time. Notice that the final value of F reflects the fact that μ_w is not zero. Consequently, the final values of the angles (φ, ϑ, ψ) are different from zero and not constant.

Fig. 8 shows the evolution of the estimator $\hat{\mu}_c(t)$ and of the estimation error $\tilde{\mu}_c$. Fig. 9 depicts the evolution in time of the angular velocity that is controlled by the inner-loop. Fig. 10 shows a comparison of the controller with the unknown force estimator against the controller without the estimator with the same gains and in the presence of an unknown constant force given by $\mu_c = [2 \ 2 \ 0]^T$.

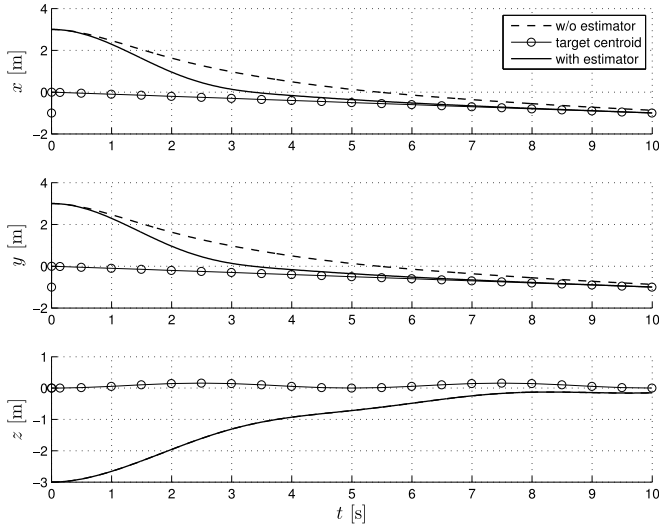


Fig. 10. Comparison of the controller with the unknown force estimator versus the controller without the estimator, in the presence of an unknown force.

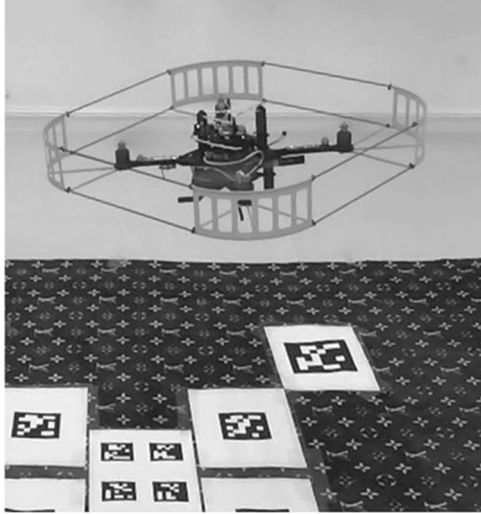


Fig. 11. Quadrotor vehicle used in the experimental setup.

VI. EXPERIMENTAL RESULTS

In order to experimentally validate the proposed control algorithms, we developed a rapid prototyping and testing architecture using a MATLAB/Simulink environment to seamlessly integrate the sensors and the camera, the control algorithm, and the communication with the vehicle. The controller is developed and tuned in a MATLAB environment, and as a final step, C code is generated and compiled to run onboard the vehicle. Fig. 12 depicts the hardware stack and communications scheme of the experimental setup, with all the relevant software running on-board. The vehicle used for the experiments is an Asctec Pelican quadrotor [36], depicted in Fig. 11. The particular aerial vehicle used for the experiments is equipped with a wide-angle camera facing the ground and an onboard computer used for image processing. Commanded through a robust inner-loop controller running on a dedicated microprocessor, it is an ideal platform

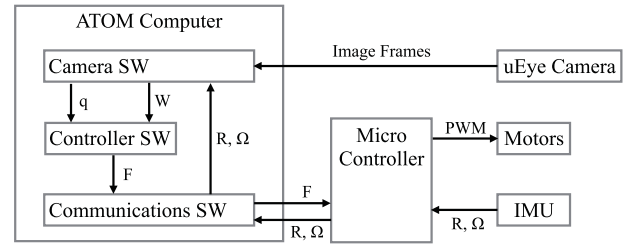


Fig. 12. Flowchart with onboard hardware and software components and communication links.

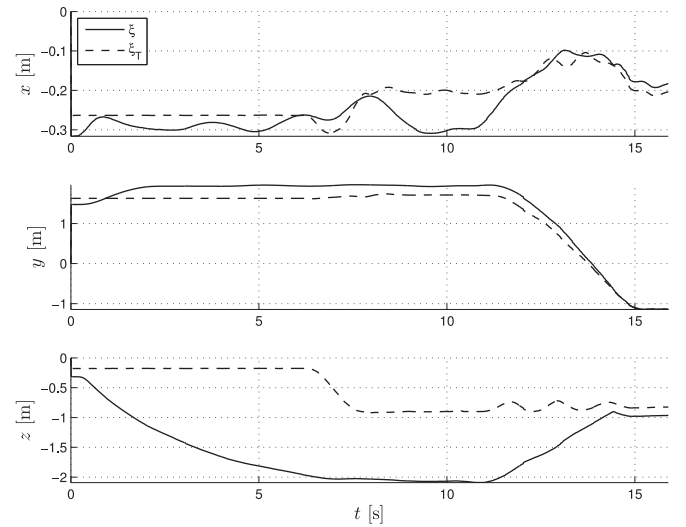


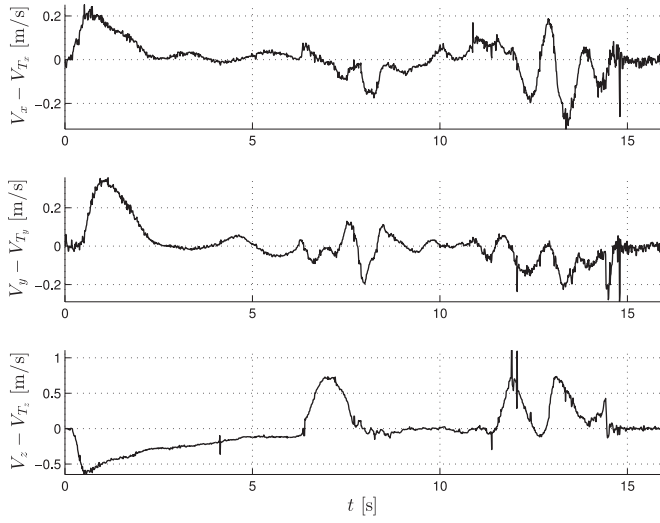
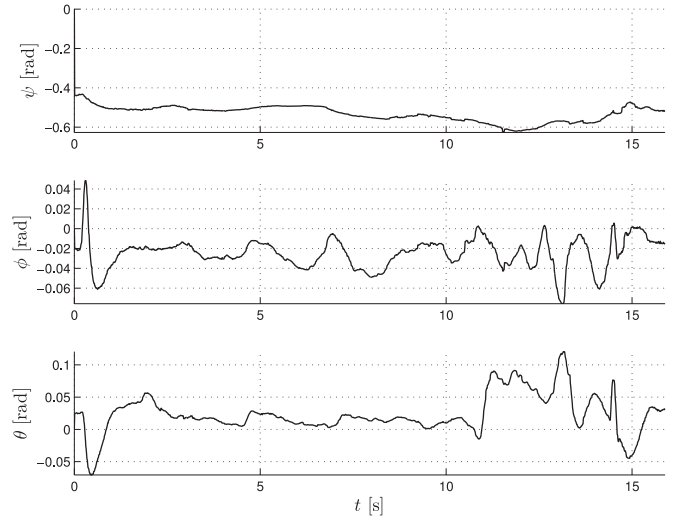
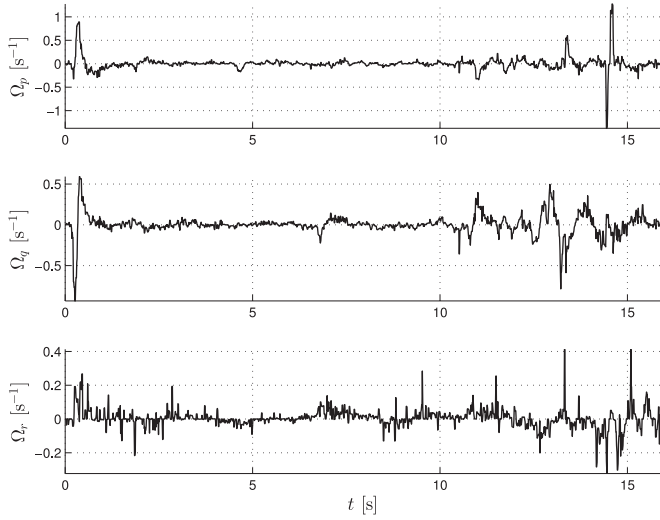
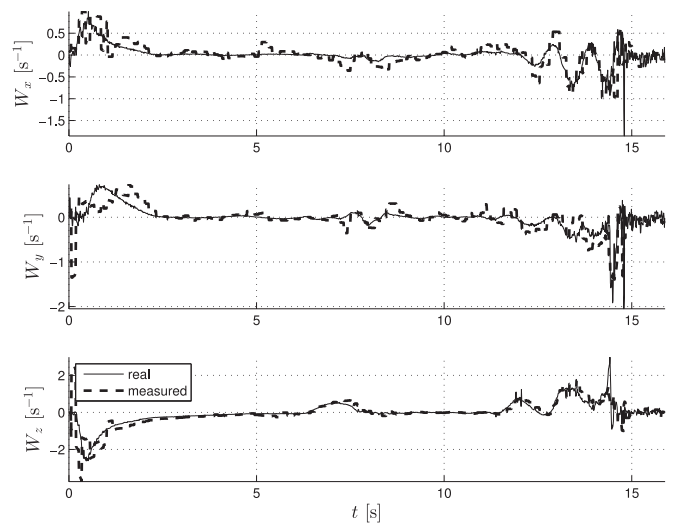
Fig. 13. Position $\xi(t)$ of the center of mass of the vehicle (solid lines) and position of the centroid $\xi_T(t)$ (dashed lines).

for implementing the controllers proposed in the present work. The quadrotor weighs 1275 g with battery included and the arm length from the center of mass to each motor is 20 cm. The available commands are thrust force and attitude, or, equivalently, the force F provided by the outer-loop controller (17).

The onboard computer (a single-core Intel Atom Z530 running at 1.6 GHz) is running a linux operating system and runs three major software components responsible for the

- 1) interface with the camera hardware, image acquisition, landmark identification, and optical flow computation;
- 2) computation of force references from the landmarks and translational optical flow;
- 3) interface with the microprocessor, receiving IMU data and sending force references to the inner-loop controller (see Fig. 12).

The camera is a uEye UI-1221LE featuring a 1/3-in sensor with global shutter, maximum resolution of 752×480 pixel, and is provisioned with a 2.2-mm lens. To expedite development time, we opted to use the ARToolkit Plus library for detecting the landmarks, which in this case are ARTags [37]. Notice, however, that, although the relative camera position and orientation can be obtained from ARTags, we are only using the directions to the landmarks as required by the control law. In fact, a more

Fig. 14. Velocity error ($V(t) - V_T(t)$).Fig. 16. Euler angles ($\varphi(t), \vartheta(t), \psi(t)$).Fig. 15. Angular velocity $\Omega(t)$.Fig. 17. Translational optical flow $W(t)$. Solid line represents the translational optical flow computed from the image sequence. Dashed line represents the translational optical flow ground truth provided by the VICON system.

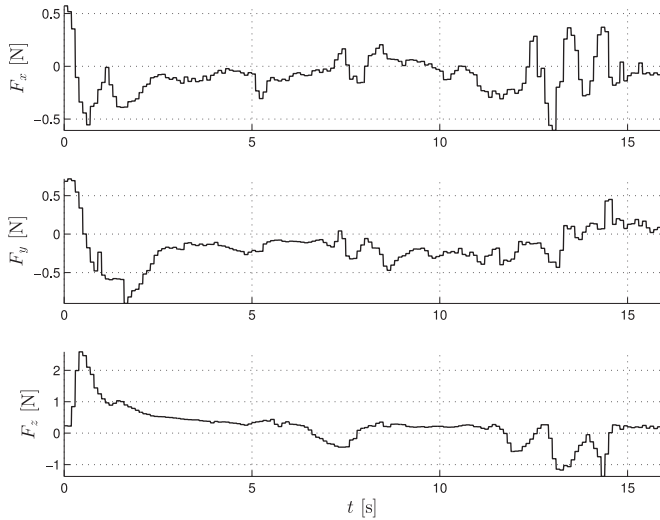
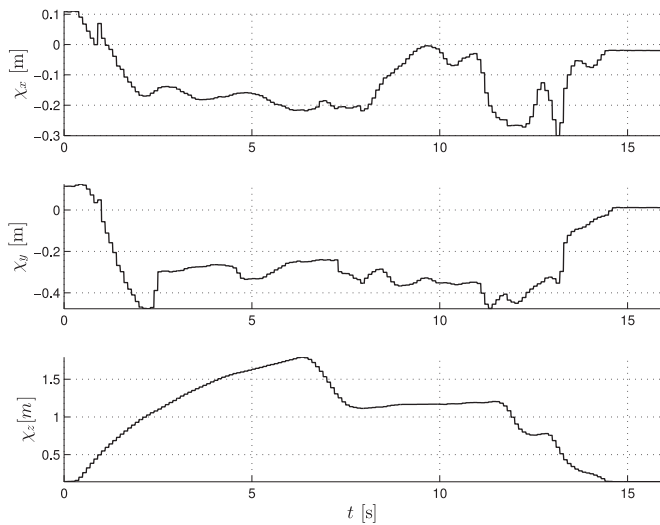
simplistic landmark detection algorithm could be used to detect some unknown sized landmarks, such as circumferences.

The translational optical flow is also computed onboard. The computation is based on the optical flow field provided by a pyramidal implementation of the Lucas–Kanade algorithm [32]. As described in Section III, the flow field is projected onto a section of a sphere, and the resulting average of the projected vectors, ϕ_w , is used to compute the translational optical flow using (15).

A VICON Bonita motion capture system [24], comprising 12 cameras, is used together with markers attached to the quadrotor and to the target plane, in order to provide ground truth measurements and evaluate the performance of the proposed control law. The motion capture system is able to accurately locate the positions of the markers, from which it obtains position and orientation measurements. VICON Bonita is a high-performance system, able to operate with submillimeter and subdegree preci-

sion at 100 Hz. The performance of the motion capture system is such that the linear and angular velocities are well estimated from the position and attitude measurements by a simple backwards Euler difference, with relatively low noise level. The computer running the VICON Tracker motion capture software is an Intel Core i7 running at 3.1 GHz.

The experiments were conducted with the same gains as in the simulations. The positions of the vehicle and target plane expressed in $\{T\}$, ξ and $\xi_T = 1/n \sum_i s_i$, respectively, are shown in Fig. 13. The evolution of the velocity error in $\{B\}$ and angular velocity is depicted in Figs. 14 and 15, respectively. In the figures, the landing maneuver is triggered at $t \approx 6$ s. From $t = 0$ s to $t \approx 6$ s, the vehicle is controlled by a simple hover controller that stabilizes position at $\xi = [-0.25 \ 1.93 \ -2]$ m using the VICON measurements for feedback. The target plane is moving

Fig. 18. Controller output $F(t)$.Fig. 19. Position error expressed in body coordinates $\chi(t)$.

at a random velocity, oscillating in the z -direction, similarly to the movement presented in the simulations. A video of some of the trials is available at [38]. The orientation of the vehicle described by the Euler angles is depicted in Fig. 16. Fig. 17 shows a comparison between the onboard measured translational optical flow and the ground truth $(V(t) - V_T(t))/d(t)$ provided by the motion capture system. The controller output force F is illustrated in Fig. 18. The state $\chi(t)$, obtained by the VICON system, is depicted in Fig. 19.

The translational optical flow computed from the image sequence is visibly noisy and its extraction is computationally heavy; nevertheless, the vehicle is able to perform the maneuver safely. On the Atom processor we were only able to run the optical flow computations at a rate of 10 Hz, but it is possible to improve on these results by augmenting the computational capability of the vehicle's onboard system and by improving the camera/lenses system. The landing maneuver is complete

when the vehicle touches the landing platform; however, there is no direct method to decide when is the right moment to shut down the motors. A routine that detects the touchdown moment using the accelerometers is implemented for this purpose and validated on-the-fly against the VICON measurements in order to safely turn down the motors.

VII. CONCLUSION AND FUTURE RESEARCH

This paper has addressed the problem of landing a VTOL vehicle on a moving target. The proposed controller uses only a common sensor suite for this type of vehicles, which is composed of an onboard camera and an IMU sensor. The kinematics of the system are represented in terms of image features and translational optical flow, and as a consequence, input actuation is dependent on an unmeasured height that varies dynamically with the vehicle's movement. The image features are used in a way that allows for stabilization without the need to estimate parameters related to the unknown height. The control law includes also an estimator for constant, or slowly time-varying, unknown inertial forces.

The proof of convergence of the overall control scheme is provided and the simulation results show the effectiveness of the control algorithm in perfect conditions. The experiment results show the behavior in an indoor scenario.

Future work includes studying the application of similar algorithms on other types of vehicles such as fixed-wing aircraft as well as conducting experiments outdoors under the influence of wind disturbances.

REFERENCES

- [1] *Unmanned Aircraft Systems: Perceptions & Potential*, Aerosp. Ind. Assoc., Arlington, VA, USA, 2013.
- [2] M. Zuckerberg, *Connecting the world from the sky*, accessed Mar. 2014. [Online]. Available: <http://www.internet.org/projects>
- [3] P. Batista, C. Silvestre, and P. Oliveira, "Sensor-based globally asymptotically stable filters for attitude estimation: Analysis, design, and performance evaluation," *IEEE Trans. Autom. Control*, vol. 57, no. 8, pp. 2095–2100, Aug. 2012.
- [4] R. Mahony, T. Hamel, and J.-M. Pflimlin, "Nonlinear complementary filters on the special orthogonal group," *IEEE Trans. Autom. Control*, vol. 53, no. 5, pp. 1203–1218, Jun. 2008.
- [5] M. K. Kaiser, N. Gans, and W. Dixon, "Vision-based estimation for guidance, navigation, and control of an aerial vehicle," *IEEE Trans. Aerosp. Electron. Syst.*, vol. 46, no. 3, pp. 1064–1077, Jul. 2010.
- [6] J. Lobo and J. Dias, "Vision and inertial sensor cooperation using gravity as a vertical reference," *IEEE Trans. Pattern Anal. Mach. Intell.*, vol. 25, no. 12, pp. 1597–1608, Dec. 2003.
- [7] F. Chaumette and S. Hutchinson, "Visual servo control. I. Basic approaches," *IEEE Robot. Autom. Mag.*, vol. 13, no. 4, pp. 82–90, Dec. 2006.
- [8] F. Chaumette and S. Hutchinson, "Visual servo control. II. advanced approaches [tutorial]," *IEEE Robot. Autom. Mag.*, vol. 14, no. 1, pp. 109–118, Mar. 2007.
- [9] P. Corke and M. Good, "Dynamic effects in visual closed-loop systems," *IEEE Trans. Robot. Autom.*, vol. 12, no. 5, pp. 671–683, Oct. 1996.
- [10] R. Kelly, R. Carelli, O. Nasisi, B. Kuchen, and F. Reyes, "Stable visual servoing of camera-in-hand robotic systems," *IEEE/ASME Trans. Mechatronics*, vol. 5, no. 1, pp. 39–48, Mar. 2000.
- [11] S. Hutchinson, G. Hager, and P. Corke, "A tutorial on visual servo control," *IEEE Trans. Robot. Autom.*, vol. 12, no. 5, pp. 651–670, Oct. 1996.
- [12] R. Mahony, P. Corke, and T. Hamel, "Dynamic image-based visual servo control using centroid and optic flow features," *J. Dyn. Syst., Meas. Control*, vol. 130, no. 1, 2008, Art. 011005.

- [13] O. Bourquardez, R. Mahony, N. Guenard, F. Chaumette, T. Hamel, and L. Eck, "Image-based visual servo control of the translation kinematics of a quadrotor aerial vehicle," *IEEE Trans. Robot.*, vol. 25, no. 3, pp. 743–749, Jun. 2009.
- [14] J. Thomas, G. Loianno, K. Sreenath, and V. Kumar, "Toward image based visual servoing for aerial grasping and perching," in *Proc. 2014 IEEE Int. Conf. Robot. Autom.*, May 2014, pp. 2113–2118.
- [15] C. McCarthy and N. Barnes, "A unified strategy for landing and docking using spherical flow divergence," *IEEE Trans. Pattern Anal. Mach. Intell.*, vol. 34, no. 5, pp. 1024–1031, May 2012.
- [16] A. Beyeler, J.-C. Zufferey, and D. Floreano, "OptiPilot: Control of take-off and landing using optic flow," in *Proc. Eur. Micro Air Veh. Conf. Competition*, 2009, pp. 1–8.
- [17] S. Zingg, D. Scaramuzza, S. Weiss, and R. Siegwart, "MAV navigation through indoor corridors using optical flow," in *Proc. IEEE Int. Conf. Robot. Autom.*, 2010, pp. 3361–3368.
- [18] B. Hérissé, F.-X. Russotto, T. Hamel, and R. Mahony, "Hovering flight and vertical landing control of a VTOL unmanned aerial vehicle using optical flow," in *Proc. IEEE/RSJ Int. Conf. Intell. Robots Syst.*, Sep. 2008, pp. 801–806.
- [19] P. Serra, F. Le Bras, T. Hamel, C. Silvestre, and R. Cunha, "Nonlinear IBVS controller for the flare maneuver of fixed-wing aircraft using optical flow," in *Proc. 49th IEEE Conf. Decis. Control*, Dec. 2010, pp. 1656–1661.
- [20] T. S. Richardson, "Automated vision-based recovery of a rotary wing unmanned aerial vehicle onto a moving platform," *J. Field Robot.*, vol. 30, no. 5, pp. 667–684, 2013.
- [21] T. Hamel and R. Mahony, "Visual servoing of an under-actuated dynamic rigid-body system: An image-based approach," *IEEE Trans. Robot. Autom.*, vol. 18, no. 2, pp. 187–198, Apr. 2002.
- [22] B. Hérissé, T. Hamel, R. Mahony, and F.-X. Russotto, "Landing a vtol unmanned aerial vehicle on a moving platform using optical flow," *IEEE Trans. Robot.*, vol. 28, no. 1, pp. 77–89, Feb. 2012.
- [23] P. Serra, R. Cunha, T. Hamel, D. Cabecinhas, and C. Silvestre, "Landing on a moving target using image-based visual servo control," in *Proc. 53rd IEEE Conf. Decis. Control*, Dec. 2014, pp. 2179–2184.
- [24] VICON, Motion capture systems from vicon, 2014. [Online]. Available: <http://www.vicon.com>
- [25] A. Tayebi and S. McGilvray, "Attitude stabilization of a VTOL quadrotor aircraft," *IEEE Trans. Control Syst. Technol.*, vol. 14, no. 3, pp. 562–571, May 2006.
- [26] N. Guenard, T. Hamel, and M. V., "Dynamic modeling and intuitive control strategy for an "X4-flyer"," in *Proc. Int. Conf. Control Autom.*, Jun. 2005, pp. 141–146.
- [27] G. M. Hoffmann, H. Huang, S. L. Wasl, and E. C. J. Tomlin, "Quadrotor helicopter flight dynamics and control: Theory and experiment," in *Proc. AIAA Guid., Navig., Control Conf.*, 2007, pp. 1–20.
- [28] P. Pounds, R. Mahony, P. Hynes, and J. Roberts, "Design of a four-rotor aerial robot," in *Proc. Aust. Conf. Robot. Autom.*, Nov. 2002, pp. 145–150.
- [29] R. Ghanadan, "Nonlinear control system design via dynamic order reduction," in *Proc. 33rd IEEE Conf. Decis. Control*, 1994, vol. 4, pp. 3752–3757.
- [30] R. Sepulchre, M. Janković, and P. Kokotović, *Constructive Nonlinear Control*, ser. Communications and Control Engineering. Berlin, Germany: Springer, 1997.
- [31] J. Koenderink and A. Doorn, "Facts on optic flow," *Biol. Cybern.*, vol. 56, no. 4, pp. 247–254, 1987.
- [32] B. D. Lucas and T. Kanade, "An iterative image registration technique with an application to stereo vision," in *Proc. 7th Int. Joint Conf. Artif. Intell.*, 1981, pp. 674–679.
- [33] Open source computer vision library. [Online]. Available: <http://opencv.org>. Accessed on Mar. 20, 2014.
- [34] D. Honegger, L. Meier, P. Tanskanen, and M. Pollefeys, "An open source and open hardware embedded metric optical flow CMOS camera for indoor and outdoor applications," in *Proc. IEEE Int. Conf. Robot. Autom.*, May 2013, pp. 1736–1741.
- [35] Px4flow smart camera. (2016). [Online]. Available: <https://pixhawk.org/modules/px4flow>
- [36] Asctec, Ascending technologies. (2016). [Online]. Available: <http://www.asctec.de>
- [37] D. Wagner and D. Schmalstieg, "Artoolkitplus for pose tracking on mobile devices," in *Proc. 12th Comput. Vis. Winter Workshop*, 2007, pp. 139–146.
- [38] P. Serra, R. Cunha, T. Hamel, D. Cabecinhas, and C. Silvestre, *Landing on a moving target using dynamic image-based visual servo control*, accessed Jun. 2015. [Online]. Available: <http://isr.tecnico.ulisboa.pt/pserra/media/flomt.mp4>



Pedro Serra received the B.Sc., M.Sc., and Ph.D. degrees in electrical and computer engineering from Instituto Superior Técnico, Universidade de Lisboa, Lisboa, Portugal, in 2006, 2007, and 2016, respectively.

He was a Research Assistant with the Faculty of Science and Technology, University of Macau, Macao, China, from 2013 to 2015. He is currently a Control Specialist with the Space Systems Business Unit, GMV Aerospace and Defense, Madrid, Spain. His research interests include nonlinear control, vision-based control systems, and controller design for autonomous vehicles.



Rita Cunha received the Licenciatura degree in information systems and computer engineering and the Ph.D. degree in electrical and computer engineering from Instituto Superior Técnico (IST), Universidade de Lisboa, Lisboa, Portugal, in 1998 and 2007, respectively.

She is an Assistant Researcher with the Institute for Systems and Robotics, LARSyS, Lisbon, and an Invited Assistant Professor with the Department of Electrical and Computer Engineering, IST. Her research interests include nonlinear systems and control and vision-based and laser-based control with application to unmanned aerial vehicles.



Tarek Hamel received the Ph.D. degree in robotics from University of Technology of Compiègne (UTC), Compiègne, France, in 1996.

After two years as a Research Assistant with UTC, he joined Centre d'Etudes de Mécanique d'Ile de France in 1997 as an Associate Professor. He has been a Professor with University of Nice Sophia Antipolis, Nice, France, since 2003. His research interests include nonlinear control theory, estimation, and vision-based control with applications to unmanned aerial vehicles.

Prof. Hamel has served as an Associate Editor for IEEE TRANSACTIONS ON ROBOTICS and *Control Engineering Practice*.



David Cabecinhas received the Licenciatura and Ph.D. degrees in electrical and computer engineering from Instituto Superior Técnico (IST), Universidade de Lisboa, Lisboa, Portugal, in 2006 and 2014, respectively.

He has been a Researcher with the Laboratory of Robotics and Systems in Engineering and Science, Institute for Systems and Robotics, IST, since 2007. He is also a Postdoctoral Fellow with the Faculty of Science and Technology, University of Macau, Taipa, Macau. His research interests include nonlinear control, sensor-based and vision-based control with applications to autonomous aerial and surface vehicles, and modeling and identification of aerial and surface vehicles.



Carlos Silvestre received the Licenciatura degree in electrical engineering, the M.Sc. degree in electrical engineering, and the Ph.D. degree in control science all from Instituto Superior Técnico (IST), Universidade de Lisboa, Lisboa, Portugal, in 1987, 1991, and 2000, respectively. He then received the Habilitation in electrical engineering and computers, also from IST, in 2011.

Since 2000, he has been with the Department of Electrical Engineering, IST, where he is currently an Associate Professor of control and robotics. Since 2015, he has been a Professor with the Department of Electrical and Computers Engineering, Faculty of Science and Technology, University of Macau, Taipa, Macau. Over the past years, he has conducted research on the subjects of navigation, guidance, and control of air and ocean robots. His research interests include linear and nonlinear control theory, hybrid control, sensor-based control, coordinated control of multiple vehicles, networked control systems, fault detection and isolation, and fault-tolerant control.